*Acta Geologica Polonica*, Vol. 75 (2025), No. 2, e43
DOI: 10.24425/agp.2024.152665

# Interpretation of the sedimentary environment of the Turonian–Coniacian Khasib Formation, using geochemical and petrological analyses

RANA ABBAS ALI

*Department of Geology, College of Science, University of Baghdad, Iraq;*
*e-mail: rana.ali@sc.uobaghdad.edu.iq*

## ABSTRACT:

Rana, A.A. 2025. Interpretation of the sedimentary environment of the Turonian–Coniacian Khasib Formation, using geochemical and petrological analyses. *Acta Geologica Polonica*, **75** (2), e43.

In this study, seven core carbonate samples were collected from the marine Upper Cretaceous (Turonian–Coniacian) limestone in two wells in the East Baghdad Oilfield of the Mesopotamian Basin. The Turonian–Coniacian period is regarded as the archetypal warm interval as well as a pivotal epoch in biological evolution. The carbonate strata of the Khasib Formation in the East Baghdad Oilfield of the Mesopotamian Basin were chosen as a model. The paleoenvironment was reconstructed using petrological characteristics and concentrations of major, trace, and rare earth elements (REEs), as well as carbon, oxygen, and strontium isotopic studies. The data suggest that the paleotemperature of the seawater was 28ºC, that suboxic-anoxic paleoredox conditions were present, that the paleosalinity of the seawater was minimal, and a biological explosion occurred when the temperature dropped to a point where life could survive. Dolomite dissolution, influenced by early meteoric water, established the groundwork for high-quality reservoirs, and leftover dolomite also protected natural oil. This research adds to the paleoenvironmental record and offers a theoretical foundation for future natural oil exploitation.

**Key words:** Turonian–Coniacian; Paleo-environment; Paleo-temperature; Mesopotamian Basin.

## INTRODUCTION

Recently, a number of significant carbonate reservoirs, particularly those in the Khasib Formation in the Turonian–Coniacian of the Mesopotamian Foredeep Basin, have been discovered in the East Baghdad oilfields (Al-Ameri and Al-Obaydi 2011). Many investigations have been carried out on reservoir properties (Mohammed *et al.* 2022), development strategy (Wang *et al.* 2022), and the evolutionary system (Bromhead *et al.* 2022). The paleoenvironment severely limited the formation of carbonate rocks (Besen *et al.* 2022; Yang *et al.* 2023), but little research has been done on reconstructing the Late Cretaceous in the Mesopotamian Basin (Al-Hamdani 1986; Al-Tamimi 2014; Ali and Jassim 2023). Based primarily on global stable isotopes of oxygen ($\delta^{18}O$), the predictions of low- to high latitude paleotemperature in the Late Cretaceous show an analogous pattern that emphasizes excessive warmth throughout the Turonian, a few improvements, and excessive warmth continuing into the Coniacian (Huber *et al.* 2018; Linnert *et al.* 2018). In particular, it is claimed that a number of the global temperature alterations that had an impact on ocean-climate systems with our planet's biota coincided with the shift from the hothouse in the most recent Turonian to the greenhouse during the late Campanian to Maastrichtian.

They are most probably due to rapid phytoplankton blooms caused by localized upwelling processes (Colín-Rodríguez *et al*. 2023). The average annual temperature during the Turonian–Coniacian period exceeded 14°C (Tarduno *et al*. 1998). Furthermore, $\delta^{18}$O values suggest that Late Turonian upper ocean waters were as warm as 30°C at 60°S paleolatitude (Bice *et al*. 2003). Earlier studies claimed that the average sea surface temperature during the Turonian was about 10°C higher than it is today (Wilson *et al*. 2002). These incredibly high temperatures were likely caused by CO$_2$ levels that were four to ten times greater than pre-industrial levels (Berner and Kothavala 2001).

The Turonian–Coniacian reservoir strata (Khasib Fm.) are exposed in the central Iraqi Mesopotamian Basin, where development has been relatively completed (Tukkee *et al*. 2023). This research (a) offers recent data on petrography, elements, and REE concentrations that can be used to limit the paleoenvironment; (b) explains how the Late Turonian Coniacian Event (LTCE) affected natural oil exploration in more detail.

## GEOLOGICAL SETTING

The enormous East Baghdad Oilfield (Text-fig. 1), which stretches roughly more than 100 km from northwest to southeast and has a width of more than 10 km in some places, was first discovered by the Iraq National Oil Company (INOC) in 1976 in the densely populated outskirts of Baghdad city (central Iraq) (Abdel-Fattah *et al*. 2022). A regional component of the Arabian Basin, the East Baghdad Oilfield is located in the Mesopotamian Foredeep Basin. The oilfield may be moving tectonically northeastward towards the Zagros Folding Belts along with westward movement towards the Widian Basins in the Inner Platform, whereas its southern extension is in the Mesopotamian Basin, which contains the sediments of the Tethys Sea deposited throughout the Cretaceous and Jurassic eras. The majority of that ocean's paleoenvironment was dysoxic-anoxic along the equator, and its tectonic unrest enabled the retention of high amounts of organic matter and the creation of what is now the globe's greatest natural gas and oil reser-

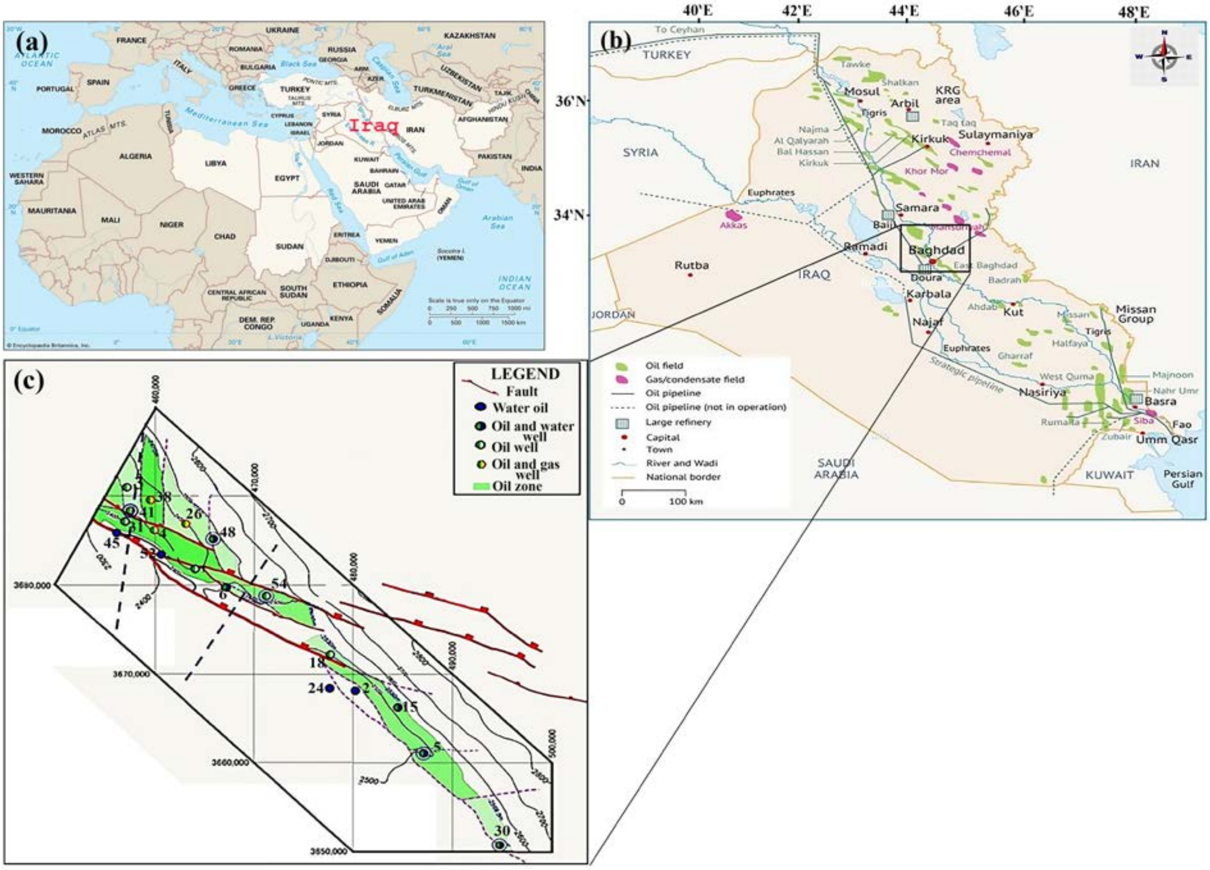

Text-fig. 1. The East Baghdad Oilfield's location. A – Iraq's geographic location. B – An Iraqi location map displaying the basins and oil fields in the northeastern Arabian Peninsula (Al-Ameri 2011). C – A map of central Iraq showing the locations of the wells used for this study (Jameel *et al*. 2020).

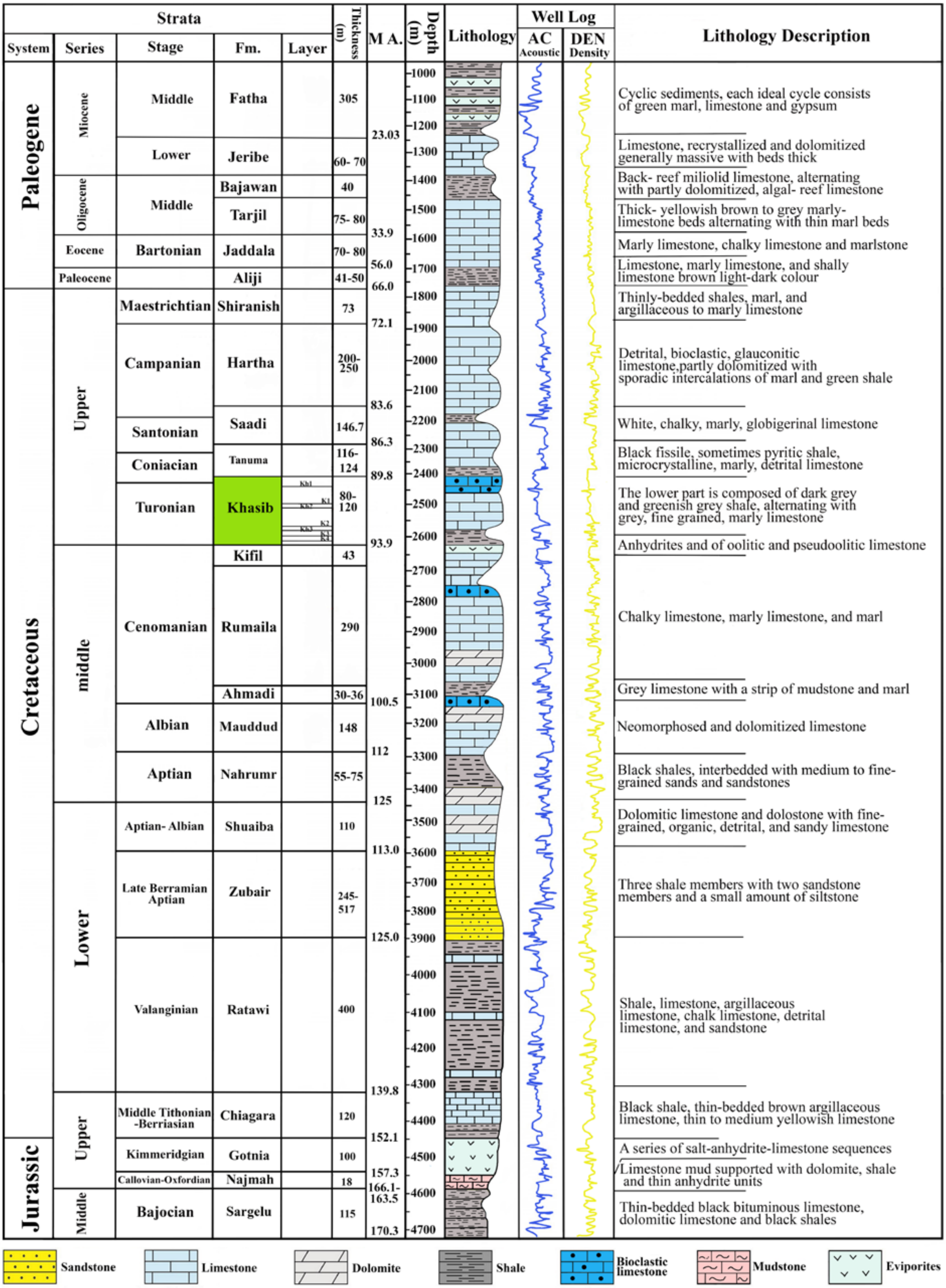

| System | Series | Stage | Fm. | Layer | Thickness (m) | M A. | Lithology Description |
|---|---|---|---|---|---|---|---|
| Paleogene | Miocene | Middle | Fatha | | 305 | 23.03 | Cyclic sediments, each ideal cycle consists of green marl, limestone and gypsum |
| | | Lower | Jeribe | | 60- 70 | | Limestone, recrystallized and dolomitized generally massive with beds thick |
| | Oligocene | Middle | Bajawan | | 40 | | Back- reef miliolid limestone, alternating with partly dolomitized, algal- reef limestone |
| | | | Tarjil | | 75- 80 | 33.9 | Thick- yellowish brown to grey marly- limestone beds alternating with thin marl beds |
| | Eocene | Bartonian | Jaddala | | 70- 80 | 56.0 | Marly limestone, chalky limestone and marlstone |
| | Paleocene | | Aliji | | 41-50 | 66.0 | Limestone, marly limestone, and shally limestone brown light-dark colour |
| Cretaceous | Upper | Maestrichtian | Shiranish | | 73 | 72.1 | Thinly-bedded shales, marl, and argillaceous to marly limestone |
| | | Campanian | Hartha | | 200-250 | 83.6 | Detrital, bioclastic, glauconitic limestone,partly dolomitized with sporadic intercalations of marl and green shale |
| | | Santonian | Saadi | | 146.7 | 86.3 | White, chalky, marly, globigerinal limestone |
| | | Coniacian | Tanuma | | 116-124 | 89.8 | Black fissile, sometimes pyritic shale, microcrystalline, marly, detrital limestone |
| | | Turonian | Khasib | Kh1<br>K1<br>Kh2<br>K2<br>Kh3<br>K3<br>K4 | 80-120 | 93.9 | The lower part is composed of dark grey and greenish grey shale, alternating with grey, fine grained, marly limestone |
| | middle | Cenomanian | Kifil | | 43 | | Anhydrites and of oolitic and pseudoolitic limestone |
| | | | Rumaila | | 290 | | Chalky limestone, marly limestone, and marl |
| | | | Ahmadi | | 30-36 | 100.5 | Grey limestone with a strip of mudstone and marl |
| | | Albian | Mauddud | | 148 | 112 | Neomorphosed and dolomitized limestone |
| | | Aptian | Nahrumr | | 55-75 | 125 | Black shales, interbedded with medium to fine-grained sands and sandstones |
| | Lower | Aptian- Albian | Shuaiba | | 110 | 113.0 | Dolomitic limestone and dolostone with fine-grained, organic, detrital, and sandy limestone |
| | | Late Berramian Aptian | Zubair | | 245-517 | 125.0 | Three shale members with two sandstone members and a small amount of siltstone |
| | | Valanginian | Ratawi | | 400 | 139.8 | Shale, limestone, argillaceous limestone, chalk limestone, detrital limestone, and sandstone |
| | Upper | Middle Tithonian -Berriasian | Chiagara | | 120 | 152.1 | Black shale, thin-bedded brown argillaceous limestone, thin to medium yellowish limestone |
| Jurassic | | Kimmeridgian | Gotnia | | 100 | 157.3 | A series of salt-anhydrite-limestone sequences |
| | | Callovian-Oxfordian | Najmah | | 18 | 166.1-163.5 | Limestone mud supported with dolomite, shale and thin anhydrite units |
| | Middle | Bajocian | Sargelu | | 115 | 170.3 | Thin-bedded black bituminous limestone, dolomitic limestone and black shales |

Text-fig. 2. The East Baghdad Oilfield’s stratigraphic column.

voir in the peninsula of Arabia (Sharland *et al.* 2001; Bromhead *et al.* 2022).

The generalized lithostratigraphic section contains marine and subordinate lagoonal beds deposited in the southern Tethys Ocean as carbonate, shale, and anhydrite sediments on a geologic time extending through the Jurassic, Cretaceous, and Paleogene up to the Middle Miocene Fatha Anhydrite (Text-fig. 2). These are contained in a 100 km long graben-horst structural system with gentle folding and normal faults that extends from the northwest to the southeast of Baghdad (Abdel-Fattah *et al.* 2022). The limestone of the Khasib Formation was deposited in a forebulge fore-slope ramp, according to microfacies and electrofacies verification and correlations. Alongside the evolved forebulge, the ramp formed above the proximal edge of the foreland basin of the Upper Cretaceous (Al-Qayim 2010; Gayara and Al Khaykanee 2015; Fayadh and Nasser 2018).

## METHODS

The major elements were analyzed using a PerkinElmer 5300DV ICP-OES. After the whole specimens had been crushed to a powdered substance, they underwent heating for one hour at 1000ºC to dissolve any remaining components using acids. The concentrations of the major elements, such as Ca, Mg, Fe, Si, and Mn, were then measured. The solutions in which the specimens had been dissolved using hydrofluoric and nitric acid at 185ºC for twenty-four hours were used to determine the trace elements using a PerkinElmer Nexion 300D ICP-MS apparatus. Additionally, various trace elements were measured, including Zr, Ti, Hf, Sr, Th, and Sc (Table 1). The dissolving techniques of Chen *et al.* (2013) were used to analyze the REEs in order to prevent the effect of non-carbonate mineral components. The materials were crushed to obtain 200-mesh powder prior to being dissolved in an acid solution ($HNO_3$ and HF) and having the composition of REE + Y determined. Additionally, analyses of the carbonate samples' stable C and O isotopic compositions were performed. A Finnigan MAT253 mass spectrometer was used to evaluate the substances indicated above. The treatment approach was similar to that reported by Lash (2018). The levels for $\delta^{13}C$ and $\delta^{18}O$ were calculated with δ per unit (‰) in relation to the Viennese-Pee Dee Belemnite (V-PDB) standard and the standards set by the Vienna Standardized Average Oceans Water (V-SMOW), respectively. The standard samples utilized were the Chinese standards GBW04415 ($\delta^{13}C$ = +1.51 ± 0.02‰, V-PDB, and $\delta^{18}O$ = -10.57 ± 0.10‰, V-PDB) and GBW04416 ($\delta^{13}C$ = -5.06 ± 0.05‰, V-PDB, and $\delta^{18}O$ = -22.15 ± 0.17‰, V-PDB). The accuracy of those standard specimens' calibration was checked after each three specimens to make sure it was better than 0.2‰.

In the Finnigan MAT Triton TI mass spectrometer, Sr isotope experiments were performed. Savillex 9.5-milliliter Teflon-PFA containers were filled with approximately one hundred milligrams of carbonate substance (using a concentration of 0.2 mg precision). Two milliliters of 0.2 M hydrochloric acid were used to dissolve each sample on a heated plate for 4 hours at 80ºC. Before centrifuging, the specimen's liquid was cooled at ambient temperature for about one hour at 5000 rpm. The excess fluid was then removed from the centrifuge tube and allowed to dry on a hotplate. The samples were then redissolved using 1.0 milliliters of 2.5 M hydrochloric acid. Next, 2 ml of AG50W-X12 cation exchange resin was added to the sample solution to load it into the resin column that had already been preconditioned for extracting Sr in the specimen matrices. The tube had been washed by seven milliliters of 5 M HCl after being rinsed using 0.5 milliliters of 2.5M hydrochloric acid four times. After that, 3.5 ml of 5 M HCl was used to remove the Sr fraction (Li *et al.* 2019). When compared to the NBS-777 reference sample, the obtained $^{87}Sr/^{86}Sr$ ratio was 0.701257 ± 0.000001.

## RESULTS

### Petrological characteristics

Carbonate rocks make up the Khasib Formation's lithology in the East Baghdad Oilfield. According to the criteria defined by Flugel (1982), intraclast biomicritic limestone, bioclastic lime mudstone, calcispheral lime mudstone, bioclastic lime wackestone, oolitic and peloidal lime grainstone, and dolomite lime mudstone have been found in the formation. The particles in the matrix of the Khasib Fm. limestones were just a few microns in size, which was small. Secondary sparry calcite and dolomite filled the cracks, which indicates late cementing, and the filling grains were large, usually measuring above 200 mm in diameter (Text-fig. 3A). Cavities were present in some bioclasts, but they are generally few. While authigenic minerals are represented by pyrite, which is found as sporadic spots (Text-fig. 3B), dolomite is one of the scattered minerals with rhombic

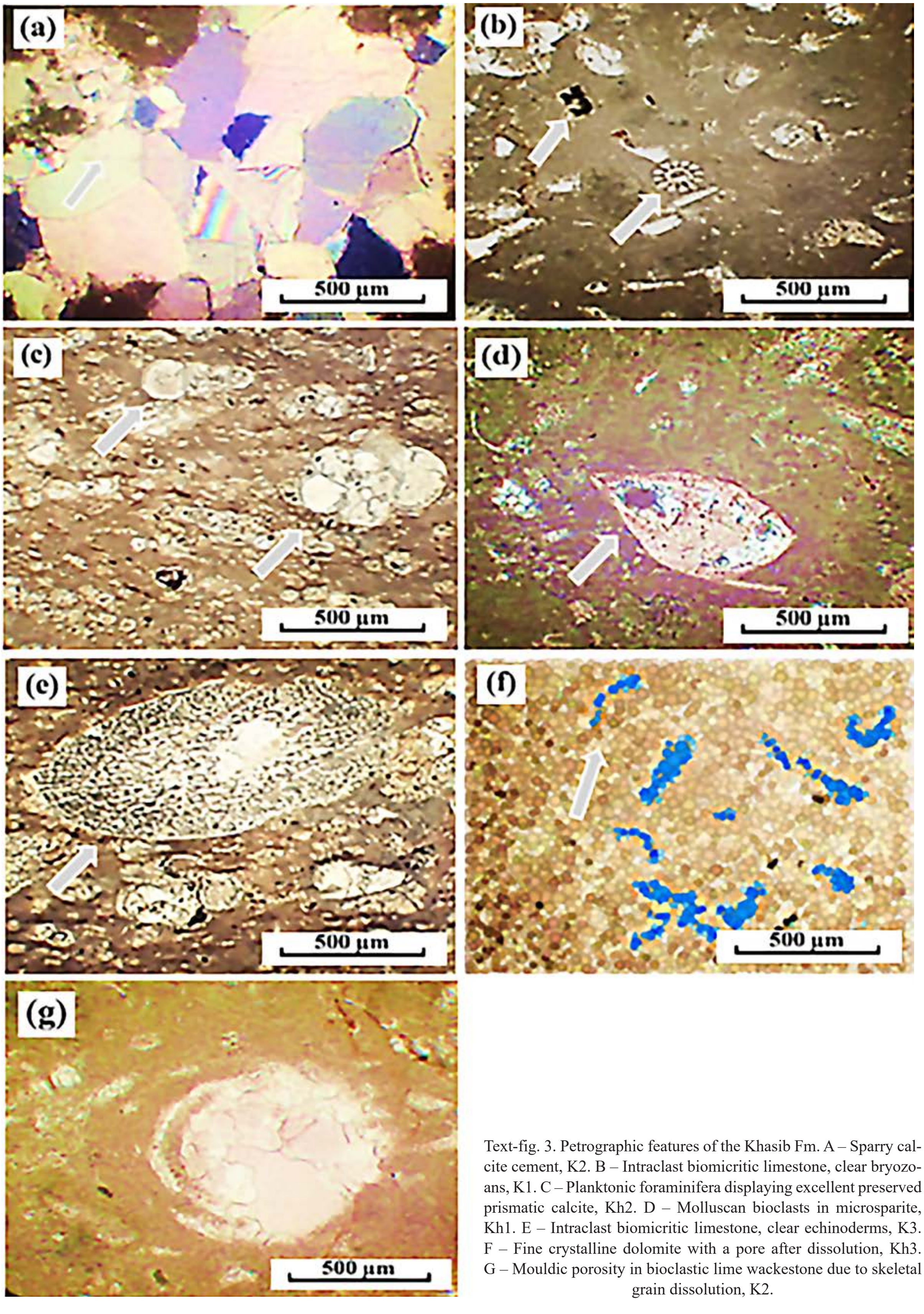

Text-fig. 3. Petrographic features of the Khasib Fm. A – Sparry calcite cement, K2. B – Intraclast biomicritic limestone, clear bryozoans, K1. C – Planktonic foraminifera displaying excellent preserved prismatic calcite, Kh2. D – Molluscan bioclasts in microsparite, Kh1. E – Intraclast biomicritic limestone, clear echinoderms, K3. F – Fine crystalline dolomite with a pore after dissolution, Kh3. G – Mouldic porosity in bioclastic lime wackestone due to skeletal grain dissolution, K2.

| Well No. | Core No. | Depth, m | Major elements composition, % | | | | | | | | | |
|---|---|---|---|---|---|---|---|---|---|---|---|---|
| | | | $SiO_2$ | $Al_2O_3$ | $Fe_2O_3$ | CaO | MgO | $Na_2O$ | $K_2O$ | $TiO_2$ | $P_2O_5$ | LOI |
| EB54 | K1 | 2572 | 7.15 | 3.55 | 0.29 | 42.0 | 0.57 | 0.15 | 0.75 | 0.19 | 0.07 | 45.0 |
| | K2 | 2520 | 3.43 | 1.09 | 0.57 | 51.54 | 1.22 | 0.11 | 0.25 | 0.04 | 0.05 | 41.2 |
| | K3 | 2626 | 7.75 | 1.72 | 0.43 | 47.42 | 0.70 | 0.15 | 0.65 | 0.05 | 0.06 | 40.57 |
| | K4 | 2603 | 4.45 | 1.57 | 0.25 | 50.4 | 0.55 | 0.07 | 0.20 | 0.07 | 0.05 | 41.5 |
| EB2 | Kh1 | 2536 | 5.54 | 1.95 | 0.44 | 49.74 | 0.85 | 0.22 | 0.17 | 0.07 | 0.05 | 40.0 |
| | Kh2 | 2497 | 6.25 | 1.78 | 0.32 | 49.72 | 0.66 | 0.05 | 0.25 | 0.06 | 0.03 | 40.24 |
| | Kh3 | 2576 | 7.24 | 3.34 | 0.27 | 45.25 | 0.82 | 0.09 | 0.09 | 0.1 | 0.07 | 41.92 |

| Well No. | Core No. | Depth, m | Trace elements composition, ppm | | | | | | | | | | | | | | | |
|---|---|---|---|---|---|---|---|---|---|---|---|---|---|---|---|---|---|---|
| | | | V | Cr | Co | Ni | Rb | Ba | Sr | Th | U | Cu | Zr | Pb | Zn | Mn | Sc | Hf |
| EB54 | K1 | 2572 | 15 | 35 | 2.75 | 50 | 7.79 | 10 | 350 | 2.05 | 4.5 | 20 | 4.2 | 0.95 | 120 | 127 | 2.25 | 1.21 |
| | K2 | 2520 | 30 | 25 | 2.52 | 45 | 4.42 | 17 | 220 | 0.74 | 2.75 | 145 | 10.5 | 2.5 | 35 | 75 | 1.12 | 0.08 |
| | K3 | 2626 | 24 | 44 | 3.35 | 35 | 5.27 | 79 | 280 | 1.25 | 3.77 | 177 | 1.5 | 1.95 | 107 | 137 | 2.0 | 0.09 |
| | K4 | 2603 | 19 | 29 | 1.74 | 40 | 9.92 | 45 | 375 | 0.35 | 3.87 | 165 | 7.43 | 4.25 | 90 | 150 | 0.94 | 0.07 |
| EB2 | Kh1 | 2536 | 33 | 27 | 3.82 | 75 | 9.35 | 20 | 400 | 0.55 | 1.09 | 188 | 2.42 | 1.77 | 25 | 173 | 1.4 | 0.09 |
| | Kh2 | 2497 | 40 | 20 | 1.35 | 80 | 7.52 | 30 | 470 | 1.12 | 1.79 | 150 | 9.45 | 3.52 | 55 | 192 | 1.07 | 0.08 |
| | Kh3 | 2576 | 28 | 18 | 3.42 | 37 | 10.52 | 25 | 330 | 3.15 | 4.42 | 120 | 3.4 | 4.5 | 95 | 93 | 1.02 | 0.14 |

Table 1. Composition of major and trace elements.

crystals that are small, pure, and homogeneous. The small crystals of dolomite found in Khasib Fm. vary in size, being mostly dispersed between a few and many microns.

Foraminifera and intraclasts were discovered in abundance (Text-fig. 3C). The majority of the skeletal particles consist of the debris of invertebrate hard parts, such as molluscs (Text-fig. 3D), crustaceans, echinoderms (Text-fig. 3E), and calcareous algae, in addition to a small percentage of benthic and planktonic foraminifera. The matrix is composed of micrite, which has a consistent texture and displays compaction and unity phenomena, along with the predominance of stylolite. Numerous cracks, solution pores, and mouldic porosity after late burial dissolution by chemically aggressive subsurface fluids were seen (Text-fig. 3F).

The Khasib Formation exhibits extensive bioturbation, especially in the chalky limestone (see below), and the majority of the common trace fossils are *Thalassinoides* isp. (Al-Qayim 2010). Burrows can often be filled with porous sediments that exhibit higher dolomitization than the neighboring rocks. Oil stains the burrows regularly (Text-fig. 4A and B). In other cases, the dolomite in the burrow fills has been replaced with anhydrite prior to hydrocarbon placement (Text-fig. 4C). *Palaeophycus* isp. (Text-fig. 4D) is another trace fossil found in the Khasib Fm., which, for instance, has been reported in the East Baghdad Oilfield (Al-Qayim 2010). Approximately ten percent of Iraqi's petroleum is found within the Upper Turonian–Lower Campanian sequence in central and southern Iraq, while ninety percent of the petroleum has been found in the Khasib Formation, with the largest important reserves being in East Baghdad. This formation, on the other hand, has significant reservoir heterogeneity, having porosity varying from 5 to 28% (Total 1984). At East Baghdad, the permeability and porosity in the formation's central bioturbated part are generally constant. Intercalated thick limestone and shales comprise bioclastic lime wackestone-lime mudstone. The bioclastic lime wackestone has the most porosity. Particularly intense dolomitization may influence the whole rock volume, decreasing primary porosity while increasing intercrystalline microporosity. The chalky appearance of this section of the Khasib Fm is most likely the result of late burial dissolution by chemically hostile subsurface waters (Morse and Mackenzie 1990). Additional diagenetic impacts involve aragonitic skeleton particle dissolution, which results in mouldic porosity (Text-fig. 3G). Fracturing, which impacts most microfacies but particularly bioclastic lime wackestone and lime mudstone (Text-fig. 3F), is a crucial factor in porosity and permeability. Microfractures could have formed as a result of tectonic movements or differential burials (Total 1984). Connected intercrystalline and intergranular pore structures in dolomite and chalky limestone, as well as burrowing systems, exhibit strong permeabilities. Microfracturing considerably increases permeability, which gets worse by dissolution. Compaction as well as, to some degree, cementation reduce total permeability.

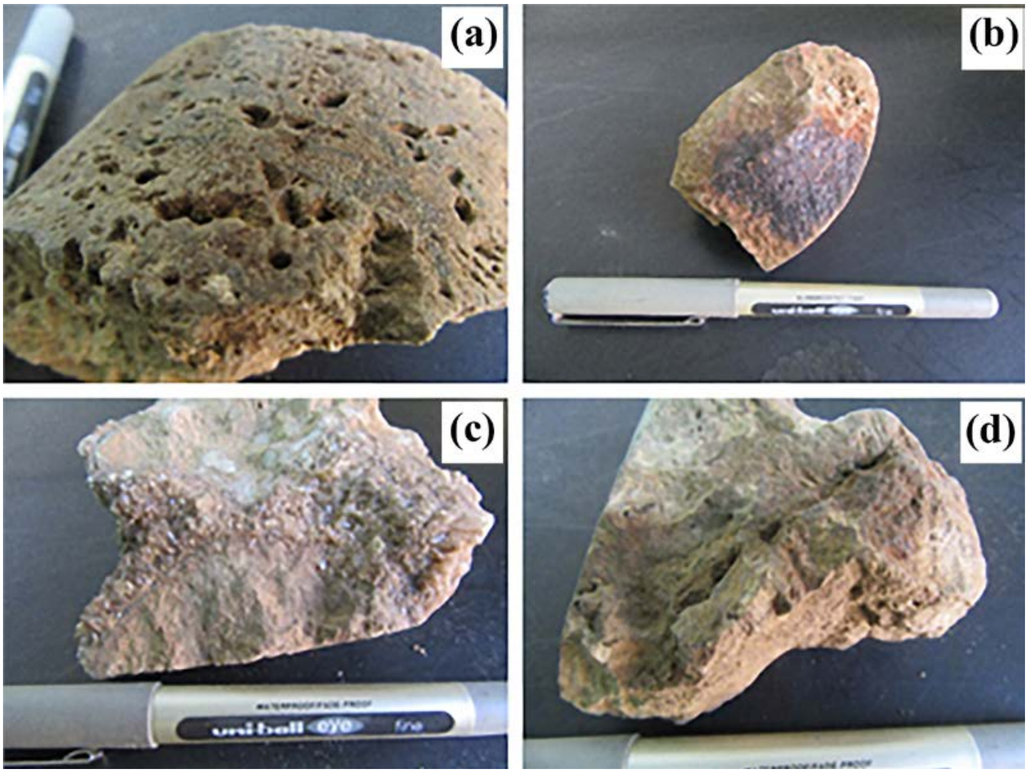

Text-fig. 4. Features of the Khasib Fm. A – Oil saturation rising outwards toward the burrow centers of porous *Thalassinoides isp.* burrows. EB54 and K3. B – Well EB54, K4 with *Thalassinoides isp.* burrows containing secondary anhydrite that precedes oil saturation. C – Dolomitized oil-saturated porous burrow fills Well EB54, K. D – *Paleophycus isp.* burrows, Well EB2, K2.

### Compositions of major and trace elements

Table 1 illustrates the findings for the investigation of the abundance of these elements. Ca and Mg were present in average concentrations of 48.01% and 0.76%, respectively. Fe and Mn content was comparatively low, with Fe lower than 0.4%, Mn lower than 136 ppm, and Al lower than 2.5%.

The average concentration for Sr is 346.42 ppm, with a range of 220 to 470 ppm. Low levels of Zr, Th, and Sc were present. Zr content was rather high, with an average of about 5.55 ppm, while Th and Sc content was essentially lesser than 2.0 ppm, with averages of about 1.31 and 1.4 ppm.

### Rare earth elements composition

The following formula is used to calculate the REE anomalies:

$$\delta Ce = 2Ce^*/ (La^* + Pr^*);\ \delta Eu = Eu^*/[(Sm^* \times Gd^*)]^{1/2};\ La^*/Yb^* = La/Yb(PAAS);\ Dy^*/Sm^* = Dy/Sm(PAAS);\ Pr^*/Sm^* = Pr/Sm(PAAS);$$

* – values have been standardized using Post Archean Australian Shale (PAAS). The REE + Y patterns, depicted in Table 2, were typically of the flattened shale kind (Text-fig. 5). These values demonstrate both depletion and enrichment patterns in comparison to the PAAS. Most limestone exhibits LREE depletion and PAAS-normalized seawater-like REE+Y trends (Ali 2023a). The samples' average REE content was low, typically less than 24 ppm, with an average of 23.24 ppm. A minimal amount of light REE enrichment was present, and overall, there was no Eu anomaly and a minimal amount of negative Ce anomaly. In general, the Y/Ho ratio was above 40 and had an average of 43.52.

### Isotopic properties

To analyze the C and O isotopes, seven samples were chosen (Table 3). The distribution of the $\delta^{13}C$ value was between -2.7 and +2.0‰, and the distribution of the $\delta^{18}O$ was between -7.4 and -4.2‰. The distribution of C isotopes is similar to that of normal seawater, but the O isotopes exhibit some negative bias, and there is a slight connection that exists between C and O isotopes (Text-fig. 6). Seven spec-

| Well No. | Core No. | Depth, m | Rare earth elements composition, ppm | | | | | | | | | | | | | |
|---|---|---|---|---|---|---|---|---|---|---|---|---|---|---|---|---|
| | | | La | Ce | Pr | Nd | Sm | Eu | Gd | Tb | Dy | Ho | Er | Tm | Yb | Lu |
| EB54 | K1 | 2572 | 4.84 | 10.7 | 1.33 | 5.72 | 0.97 | 0.23 | 1.52 | 0.15 | 0.95 | 0.2 | 0.79 | 0.11 | 0.75 | 0.21 |
| | K2 | 2520 | 2.15 | 3.52 | 0.55 | 2.37 | 0.5 | 0.1 | 1.62 | 0.14 | 0.72 | 0.15 | 0.43 | 0.05 | 0.35 | 0.05 |
| | K3 | 2626 | 3.52 | 7.0 | 0.78 | 2.92 | 0.77 | 0.2 | 0.95 | 0.13 | 0.48 | 0.17 | 0.27 | 0.07 | 0.24 | 0.07 |
| | K4 | 2603 | 1.72 | 4.7 | 0.96 | 1.95 | 0.95 | 0.17 | 0.85 | 0.09 | 0.57 | 0.05 | 0.33 | 0.06 | 0.27 | 0.04 |
| EB2 | Kh1 | 2536 | 2.82 | 6.52 | 0.92 | 1.75 | 0.57 | 0.11 | 0.59 | 0.07 | 0.55 | 0.09 | 0.41 | 0.05 | 0.25 | 0.06 |
| | Kh2 | 2497 | 2.77 | 5.57 | 0.71 | 2.19 | 0.65 | 0.09 | 0.72 | 0.1 | 0.65 | 0.13 | 0.39 | 0.04 | 0.29 | 0.05 |
| | Kh3 | 2576 | 4.79 | 10.0 | 1.55 | 2.97 | 1.09 | 0.32 | 1.5 | 0.15 | 0.98 | 0.19 | 0.52 | 0.08 | 0.34 | 0.07 |
| Well No. | Core No. | Depth, m | Rare earth elements composition, ppm | | | | | | | | | | | | | |
| | | | Y | ∑REE | δCe | δEu | Y/Ho | La*/ Yb* | Dy*/ Sm* | Pr*/ Sm* | Ni/Co | Th/U | V/ (V+ Ni) | Sr/Ba | Fe/Mn | Cr/V |
| EB54 | K1 | 2572 | 9.0 | 37.48 | 0.97 | 0.84 | 45 | 0.48 | 1.15 | 0.86 | 18.18 | 0.45 | 0.23 | 35 | 7.87 | 2.33 |
| | K2 | 2520 | 5.54 | 18.24 | 0.74 | 0.42 | 36.93 | 0.46 | 1.66 | 0.68 | 17.85 | 0.27 | 0.4 | 12.94 | 25.33 | 0.83 |
| | K3 | 2626 | 2.97 | 20.54 | 0.96 | 1.08 | 17.47 | 1.15 | 0.72 | 0.63 | 10.44 | 0.33 | 0.4 | 3.54 | 10.94 | 1.83 |
| | K4 | 2603 | 4.5 | 17.21 | 0.77 | 0.89 | 90 | 0.5 | 0.70 | 0.63 | 22.98 | 0.09 | 0.32 | 8.33 | 5.33 | 1.52 |
| EB2 | Kh1 | 2536 | 4.22 | 18.98 | 0.93 | 0.88 | 46.88 | 0.91 | 1.07 | 1.02 | 19.63 | 0.50 | 0.30 | 20 | 8.67 | 0.81 |
| | Kh2 | 2497 | 3.47 | 17.82 | 0.90 | 0.61 | 26.69 | 0.72 | 1.19 | 0.68 | 59.26 | 0.62 | 0.33 | 15.66 | 5.73 | 0.5 |
| | Kh3 | 2576 | 7.92 | 32.47 | 0.14 | 1.14 | 41.68 | 1.04 | 1.07 | 0.89 | 10.81 | 0.71 | 0.43 | 13.2 | 9.67 | 0.64 |

Table 2. Composition of rare earth elements and Y.

| Well No. | Core No. | Depth [m] | C/ O isotope composition [‰] | | | Sr isotope composition | |
|---|---|---|---|---|---|---|---|
| | | | $\delta^{13}$ $C_{V\text{-}PDB}$ | $\delta^{18}$ $O_{V\text{-}PDB}$ | $\delta^{18}$ $O_{V\text{-}SMOW}$ | $^{87}Sr/^{86}Sr$ | Standard Error |
| EB54 | K1 | 2572 | +0.9 | -4.2 | 26.5 | 0.70720 | 0.000020 |
| | K2 | 2520 | +0.7 | -7.4 | 23.2 | 0.70770 | 0.000015 |
| | K3 | 2626 | +2.0 | -5.5 | 25.2 | 0.70750 | 0.000011 |
| | K4 | 2603 | +1.0 | -6.5 | 24.1 | 0.70750 | 0.000017 |
| EB2 | Kh1 | 2536 | +0.5 | -6.5 | 24.1 | 0.70870 | 0.000015 |
| | Kh2 | 2497 | +0.5 | -5.4 | 25.3 | 0.70850 | 0.000021 |
| | Kh3 | 2576 | -2.7 | -6.2 | 24.4 | 0.70770 | / |

Table 3. Composition of C/O and Sr isotopes.

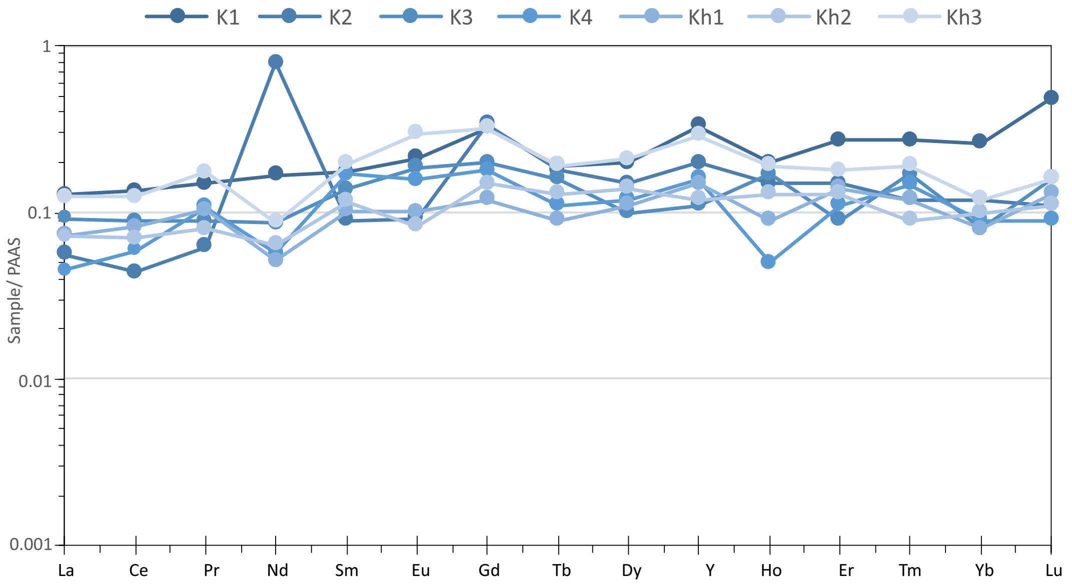

Text-fig. 5. The Khasib Fm's REE+Y properties. The PAAS's REE composition forms the foundation for standardization.

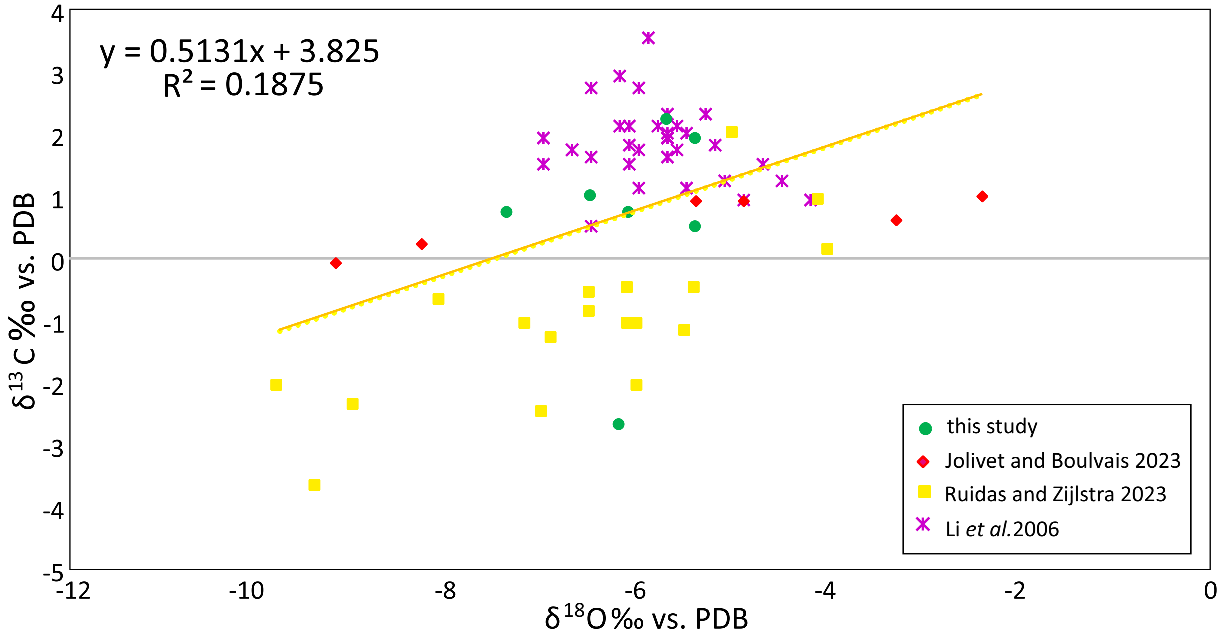

Text-fig. 6. The distribution of C and O isotopes at the Khasib Fm.

imens were chosen for Sr isotope testing, with the results ranging from 0.70720 to 0.70870, and an average of 0.70782 (Table 3). These values are comparable with the average Sr isotope values of the world's sea in the Upper Cretaceous (0.7073–0.709170, Steuber 2001, Frijia *et al.* 2015, McArthur and Howarth 2024 and references therein).

## DISCUSSION

### Assessment of contaminants

#### *Assessment of detrital contamination*

Over a long geologic period, REEs still are typically well preserved, and the properties of REEs and Y enable the definition of the initial sedimentary environments. However, at an early or a late stage of diagenesis, non-carbonate constituents like detrital inputs can easily change the REE content of carbonate rocks (Prasanta and Sarada 2021). To prevent these contaminants from changing the results, we needed to assess the level of detrital contaminants within our specimens. The initial sedimentary environment is represented by the REE + Y distribution of the original carbonate of the sample, and here the REE + Y concentration is minimal. The samples' contamination with detrital elements can be determined using the following criteria: Samples devoid of terrigenous debris show values when ∑REEs are lower than 12 ppm, Y/Ho is more than 26, Ti is lower than 0.5%, Al is lower than 1%, and Hf, Th, and Zr are lower than 20 ppm (Sarangi *et al.* 2017; Jiu *et al.* 2021). In comparison with clastic rock, the chemical deposition process will produce less Sc. The sample may be extremely contaminated when the Sc concentration exceeds 2 ppm. This investigation found that the average ∑REEs concentration was 23.24 ppm, while Ti was 0.09% or lesser, Al was 2.2% or lesser, Y/Ho was 40 or more, Zr, Th, and Hf were each less than 5 ppm, and Sc was 2 ppm or less (Table 2). The vast majority of the sample data fell in the designated "no contamination" range. The original sedimentary paleoenvironment can therefore be represented by the REE + Y concentrations measured. Terrigenous clasts continue to have a ~26 Y/Ho parameter. Despite the modest amount of terrigenous debris, the normal proportion of detrital constituents would encompass what was originally seawater; Zr, Th, Al, and Sc are especially abundant in detrital, while Y/Ho-Ce and Zr have a strong association.

$Al_2O_3$, Zr, Th, Sc, with Y/Ho have a clear negative relationship when a specific amount of detrital components is present (Duda *et al.* 2014; Sarangi *et al.* 2017), although this strong link was not evident in the scattered plot (Text-fig. 7A–D). Additionally, δCe displays weak negative correlations with $Al_2O_3$,

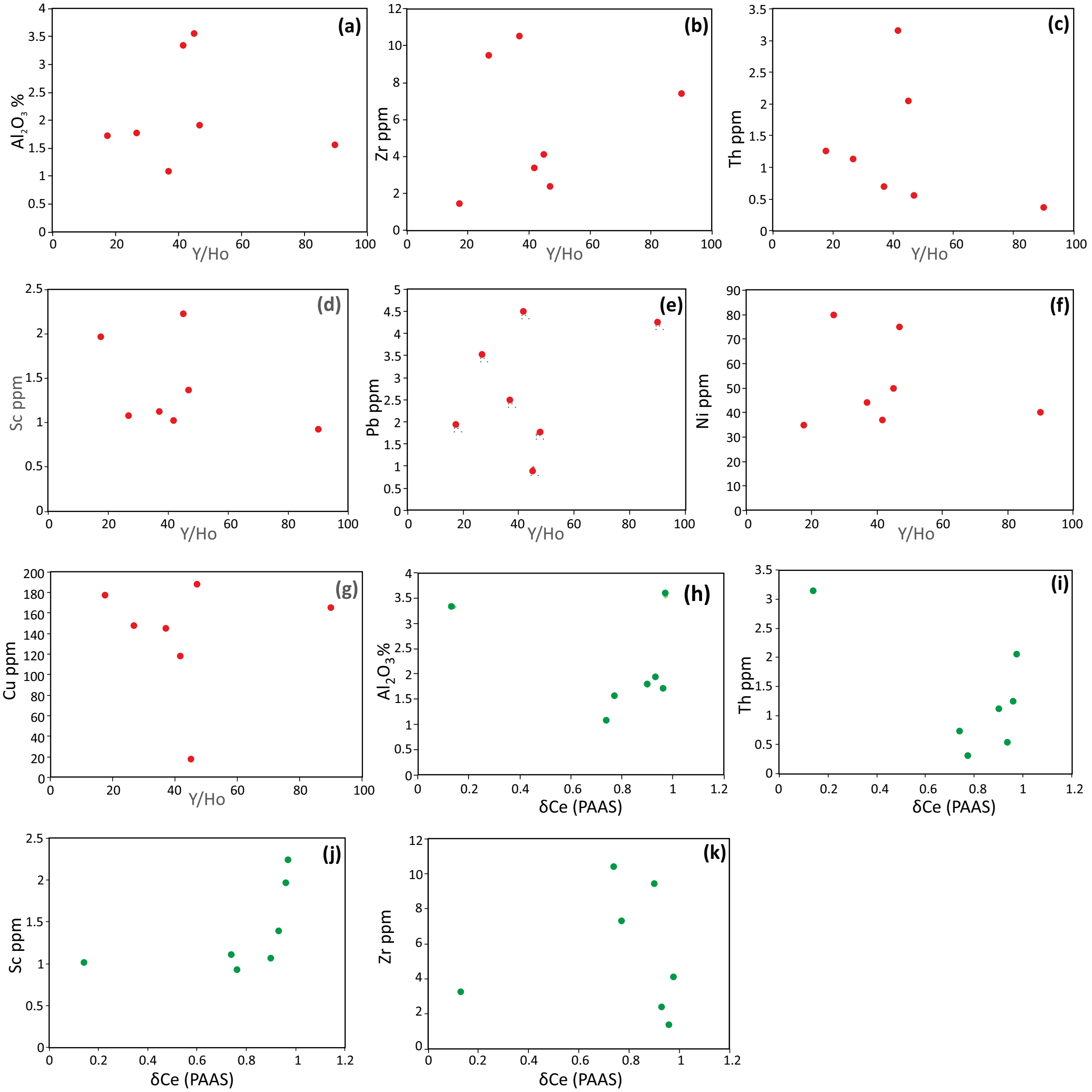

Text-fig. 7. Cross plots using carbonate geochemical information used to evaluate detrital contaminants at the Khasib Fm. $Al_2O_3$, Zr, Th and Sc show a weak negative correlation with Y/Ho, indicating the absence of a specific amounts of clastic components (A-D). δCe shows weak negative correlations with $Al_2O_3$, Th, and Zr (H, I, and K), but no correlation with Sc (J), Ni and Cu has no link with Y/Ho (F, G), so oxides had no impact on the samples, and no association among Sc and Pb with Y/Ho, indicating no sulphide consequences were possible (D and E).

Zr, and Th (Text-fig. 7H, I and K), but none with Sc (Text-fig. 7J). The changing trend caused by detritus and purified chemical deposition can be identified by the scattering plot of Y/Ho and Nd values. The samples were deposited in the region of pure chemical deposition, as can be illustrated below (Text-fig. 8). Comparable to this, seawater has very little Rb in it (usually less than 30 ppm) but is abundant in mica, feldspar, and clay minerals (Krabbenhöft *et al*. 2010). Less than 12 ppm of Rb was present in the samples from the research area (Table 1). As a result, it can be concluded that the samples from the Khasib Fm showed signs of chemical deposition and that the distribution of REEs was not influenced by detrital components.

Oxides and sulphides have an impact on carbonate precipitation that cannot be overlooked. Bolhar and Van Kranendonk (2007) and Prasanta and Sarada

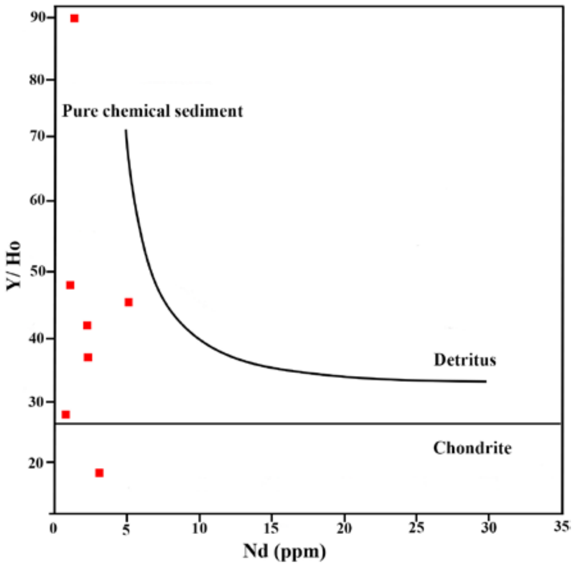

Text-fig. 8. The concentration of Y/Ho and Nd in Khasib carbonate. Detritus and chondrite trends are taken from Viehmann *et al.* (2015); low concentrations of Nd indicate the absence of detrital contamination in the samples.

(2021) employed Pb and Sc to describe the effects of sulphides, while Ni and Cu were chosen as representations for tracking oxides. Since Ni and Cu concentrations were lower and there was little to no link between them and Y/Ho (Text-fig. 7F, G), it was clear that oxides had no impact on the samples. Additionally, Text-fig. 7D and E demonstrate that there was no association among Sc and Pb with Y/Ho, meaning no sulphide consequences were possible.

Due to its long-term stability throughout geologic time, the $^{87}Sr/^{86}Sr$ ratio is usually employed to estimate changes in global sea level. Since the retaining period for Sr isotope at marine is much longer than the mixing time (about $10^6$), it won't be fractionated despite the impact of pressure, temperature, and microbes. The research area's $^{87}Sr/^{86}Sr$ ratio (Table 3) is within the range of Turonian–Coniacian seawater (McArthur and Howarth 2024 and references therein). This $^{87}Sr/^{86}Sr$ ratio should be substantially greater than seawater during the same time period if impacted by terrigenous detritus.

### *Analysis of diagenetic and metamorphic alterations*

Due to their sensitivity to post-diagenesis and metamorphism, Mn and Fe in carbonate rocks typically exhibit enrichment (Morse and Mackenzie 1990). Despite the fact that REEs may typically retain their properties during metamorphism, Ce reduction, heavy REEs reduction, and the enrichment of Eu typically happen in settings with a high water-rock ratio and elevated temperatures. Mn, Fe, δCe, and ∑REEs should therefore be negatively correlated; however, this link has not been discovered in the investigation (Text-fig. 9). The La/Yb (PAAS) ratios for the research region were often below one (with K3 = 1.15), suggesting that the elemental components reflected the initial marine water while the impact for metamorphism had been removed (Ren *et al.* 2019).

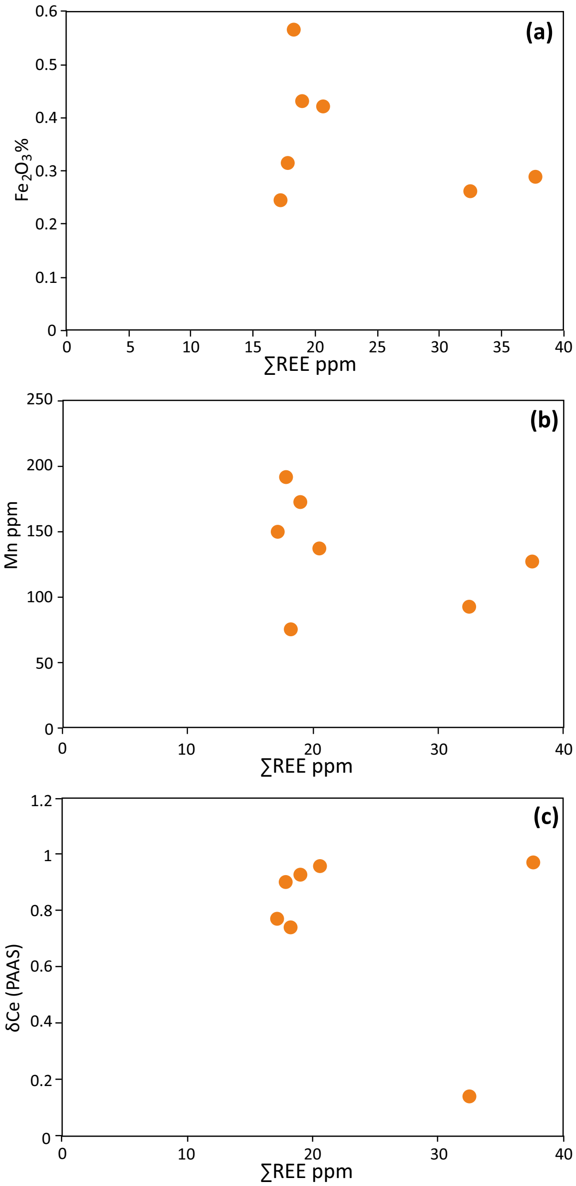

Text-fig. 9. Cross-plots for geochemical carbonate information evaluating metamorphism at the Khasib Fm. There is no relationship between the content of REEs and the metamorphism proxy $Fe_2O_3$ (A), Mn (B), and Ce (C), suggesting that metamorphism had no effect on the samples geochemical parameters.

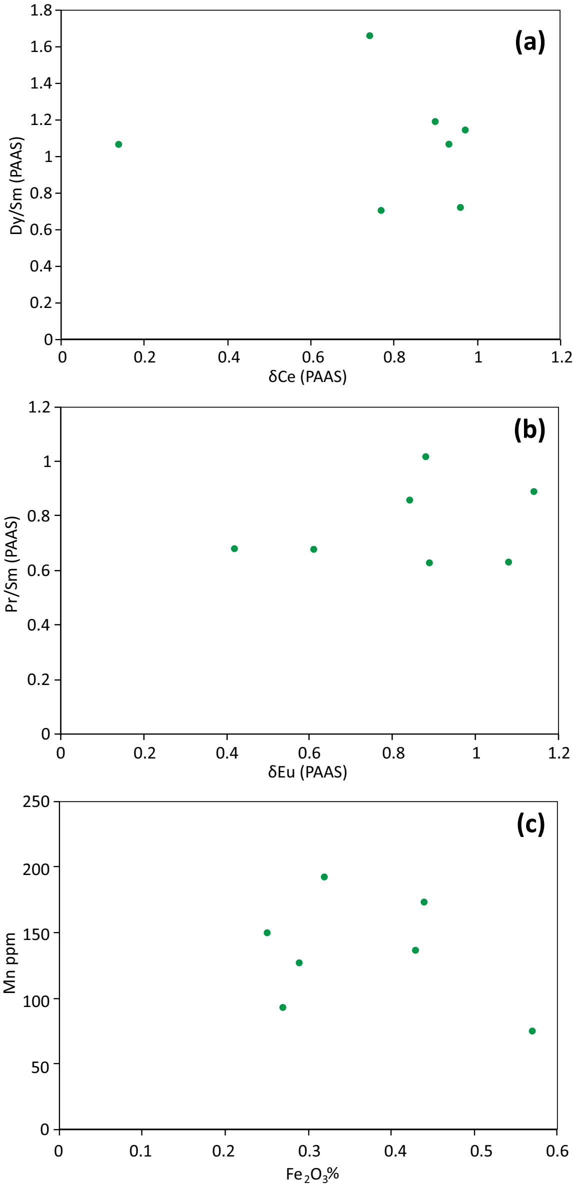

Text-fig. 10. Cross-plots for carbonate geochemical information evaluating diagenesis at the Khasib Fm. Ce and Dy/Sm (PAAS) do not correlate (A), and Eu and Pr/Sm (PAAS) have a somewhat opposite connection (B), indicating that Eu was not involved in later diagenesis, as Fe and Mn exhibit a weak out evidently positive correlation (C).

According to Al-Qayim (2010), the dolomite crystal size is often tiny, measuring only a few tens of microns (Text-fig. 3F). However, the REE+ Y distribution is not significantly impacted by either dolomitization or the late diagenetic alterations phase (Prasanta and Sarada 2021). $\delta^{18}$O is normally thought to exhibit a low isotopic composition after being exposed to meteoric water; also, whenever $\delta^{18}$O is below -10.0‰, carbonate specimens may have been influenced by fluids from hydrothermal processes (Jaffrés *et al.* 2007). In the research area, its $\delta^{18}$O had been usually less but over -10.0‰. The study's dolomite likely underwent early meteoric water dissolution based on the weak association between its C & O isotope (Text-fig. 6) and the elemental data on Fe and Mn. Nevertheless, as can be observed in Text-fig. 10A and B, there had been no association between δCe and Dy/Sm (PAAS), with a slight opposite relationship between δEu and Pr/ Sm (PAAS) suggesting the Eu didn't participate during later diagenesis (Gundogar and Sasmaz 2022). It supported the finding that there had been no Eu anomalies in the specimens that were collected. Carbonate rocks will exhibit Mn and Fe enrichment and Sr reduction during the diagenetic processes (Ali 2023b). As a result, if diagenesis were to be present, Fe and Mn should clearly be correlated positively; nevertheless, this wasn't the case in the samples (Text-fig. 10C). In summary, diagenesis had a negligibly small effect on the samples.

## Reconstruction of the paleoenvironment

The marine carbonate rocks probably retain the REE distribution which existed in their initial marine environment given the lack of evidence for subsequent diagenetic modification (Salmouna *et al.* 2014; Mehrabi *et al.* 2023).

### *Qualities of paleoredox conditions*

It is common practice to evaluate the evolution for paleoredox conditions using the proportions for the trace elements Ni/Co, U/Th, V/Cr, and V/(V + Ni) (Hussain *et al.* 2021; Ali 2023c). According to Jones and Manning (1994), oxic, dysoxic, and suboxic-anoxic environments are represented by Ni/Co ratios of <5, 5–7, and >7, respectively, while oxic, dysoxic, and suboxic-anoxic situations are indicated by V/Cr ratios of 2 and 4.25, respectively. The Th/U value is low because anoxic habitats of sedimentary deposits are abundant in U; as a result, this Th/U value is typically ~2 in seawater under anoxic circumstances and is >2 in oxic marine environments. Furthermore, the larger the proportion, the more oxic the environment is (Jeans *et al.* 2021; Yang *et al.* 2023). The clastic rock research which has been used to determine the aforementioned thresholds was numerous. Although the general pattern suggests that either an oxic or an anoxic environment is certain, the thresholds in carbonate rocks should be changed due to the comparatively low trace element abundance. The limits between

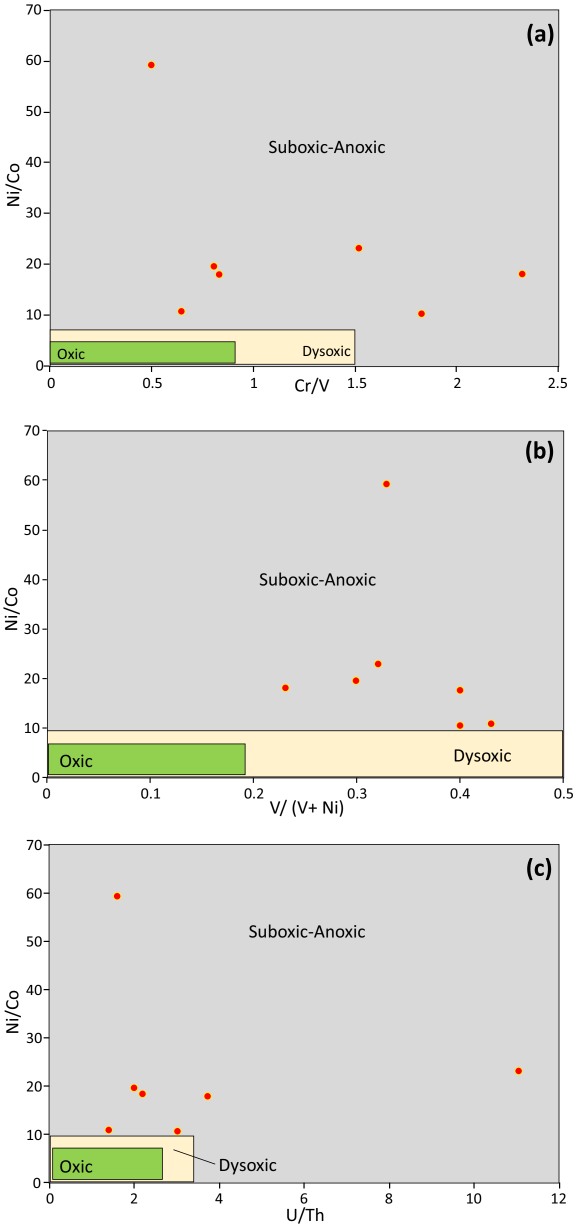

Text-fig. 11. Paleoredox phenomena in carbonate analysis diagram. The data of this study show that the paleoredox of the Khasib Fm. (Cr/V vs. Ni/Co (A), V/(V+Ni) vs. Ni/Co (B), and U/Th vs. Ni/Co (C)) is suboxic-anoxic.

oxic, dysoxic, and suboxic conditions, according to Prasanta and Sarada (2021), are V/(V+Ni) ratios of 0.3 and 0.5 in carbonate rocks and U/Th ratios of 0.2 and 0.5. The measured trace element ratios, as depicted in Text-fig. 11, were in the suboxic-anoxic zone.

A diagenetic environment's redox conditions can affect Ce. A positive Ce anomaly in minerals is caused by the tendency of $Ce^{3+}$ to shift its valence state to produce tetravalent ions in sediment under oxic conditions (Zhang and Shields 2022). This causes a clear negative Ce anomaly in the diagenetic fluid. The samples, though, clearly demonstrated a negative Ce anomaly and an average δCe of 0.77, indicating that the carbonate rocks in the Khasib Fm. were precipitated in suboxic-anoxic environments.

*Paleotemperature restoration*

The Sr/Ba ratio can be used to determine how sensitive the evaporation environment is to fluctuations in temperature in the initial sedimentary ecosystem (Jiu *et al*. 2021). The measured Sr/Ba ratio was less than 15.52, suggesting that the initial sedimentary environment was less salinous and/or under the impact of freshwater diagenesis, which was consistent with the prior conclusion (Wang *et al*. 2022). Ba and Sr appear to have no connection (Text-fig. 12A). It's important to note that there was a little positive association between Sr/Ba and REEs (Text-fig. 12B), which may suggest that there was a connection between the preservation of REEs and the development of minerals with the rise in paleotemperature. Along with the increase in ∑REEs, this might also result in an increase in the $Fe_2O_3$/MnO ratio (Text-fig. 12C). On the other hand, the research area's Sr and CaO content showed a stronger association (Text-fig. 12D). The Sr/Ca ratio is extremely sensitive to weathering and the evaporation of water (Chen *et al*. 2020), but the variation in the ratio in this research area was not significant, demonstrating that the samples were not impacted by significant weathering and evaporation of water in the last phase and that the environment for the ramp setting in this area was comparatively stable.

The computed temperature is typically that of the carbonate precipitating fluid, and the $\delta^{18}O$ value of carbonate rocks is frequently employed as a proxy for reconstructing the paleotemperature throughout the sedimentary time (Ren *et al*. 2019). The ancient seawater from the Turonian and Coniacian periods ranges in $\delta^{18}O$ from roughly -6 to -10‰, and -6.3‰ is chosen as the proxy for the average $\delta^{18}O$ of seawater (Jarvis *et al*. 2006). The average $\delta^{18}O$ measured was -5.95‰. The following equation (O'Neil *et al*. 1969) was used to get the temperature: $10^3 \ln\alpha_{calcite-water} = 2.78 \times 10^6/T^2 - 2.89$ where T is the temperature in Kelvin, and α calcite-water is the O isotope equilibrium fractionation factor between calcite and water. According to the calculations, the temperature was 28°C on average while the calcite was being formed. The actual paleotemperature should be between 24

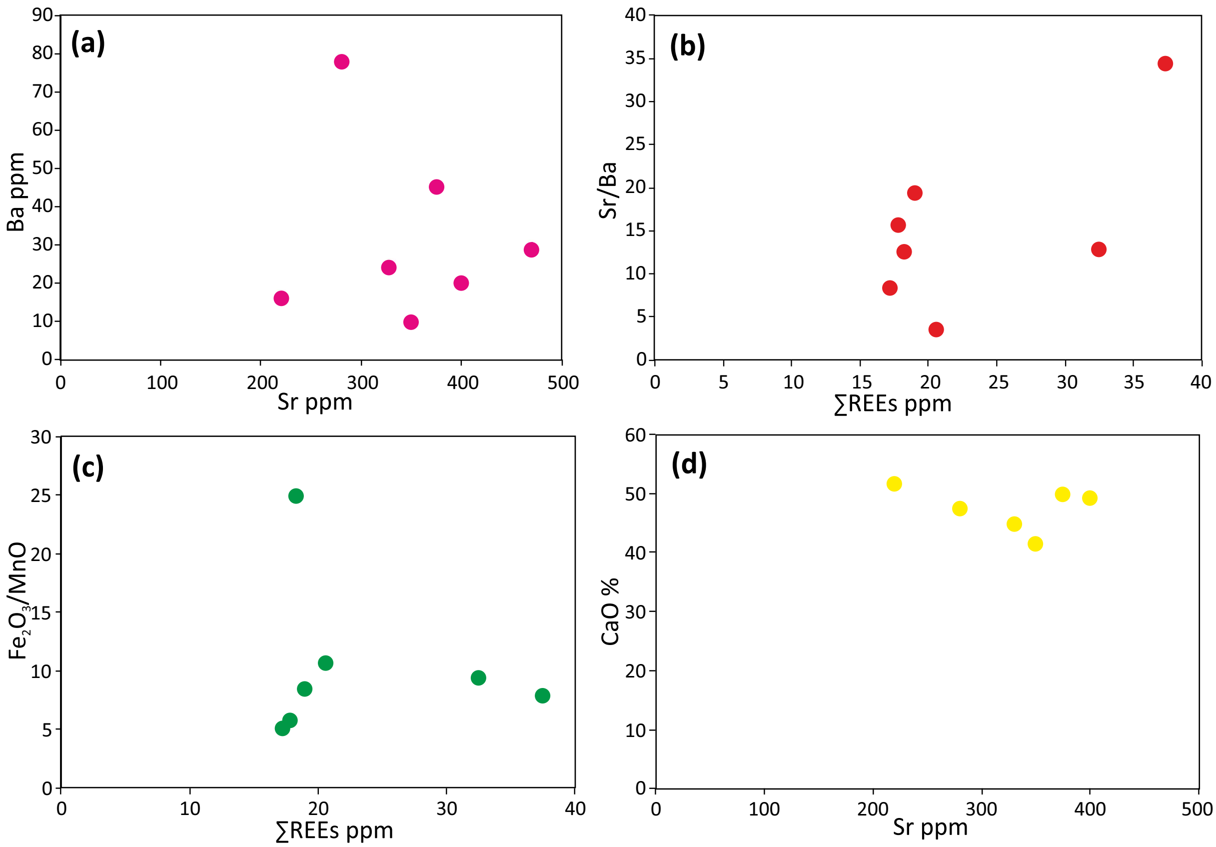

Text-fig. 12. Cross-plots of carbonate geochemical data. The measured Sr/Ba ratio is less than 15.52, suggesting that the initial sedimentary environment was less salinous, where Ba and Sr appear to have no connection (A), little positive association between Sr/Ba and REEs (B), which may suggest that there was a connection between the preservation of REEs and the development of minerals with the rise in paleotemperature. Along with the increase in REEs, may also result in an increase in the Fe2O3/MnO ratio (C), the reasearch area s Sr and CaO content showed a stronger association (D).

and 35°C, which is still close to the ocean temperature at that time (average about 30°C, Bice *et al.* 2003), taking into account that the sample measurements are somewhat impacted by early meteoric water and analytical (-5°C range) errors.

### *Paleosalinity restoration*

The Na content was utilized to represent the fluid's salinity (Geerken *et al.* 2018). The carbonate samples' average $Na_2O$ content was 0.12%, with a range of 0.05 to 0.22% (Table 1). The Na level of pure calcite deposited in the Khasib Fm was just 0.04%, according to a previous elemental investigation, showing that the salinity in the studied area was substantially lower than that in the restricted environment. As was previously mentioned, the water temperature was elevated and the sea elevation was in the transgression cycle.

### *Impact of the paleoenvironment on the isotopic carbon excursion*

A variety of factors affect the $\delta^{13}$C excursion. An increase in the productivity of marine reservoirs and the rate of weathering of the carbonate platform could both have a positive impact on the excursion (Li *et al.* 2022). The underlying idea is that the reservoir of dissolved inorganic carbon (DIC) in seawater was significantly depleted of light carbon (Saltzman and Edwards 2017). This is in line with our experimental findings, suggesting that because a large number of plankton engaged in photosynthesis during this biological explosion this may be to blame for the C isotope excursion.

When compared to the seawater temperature during the Turonian–Coniacian periods (about 30°C, Jarvis *et al.* 2006), the seawater paleotemperature in the Khasib Fm exhibits a close pattern that is compa-

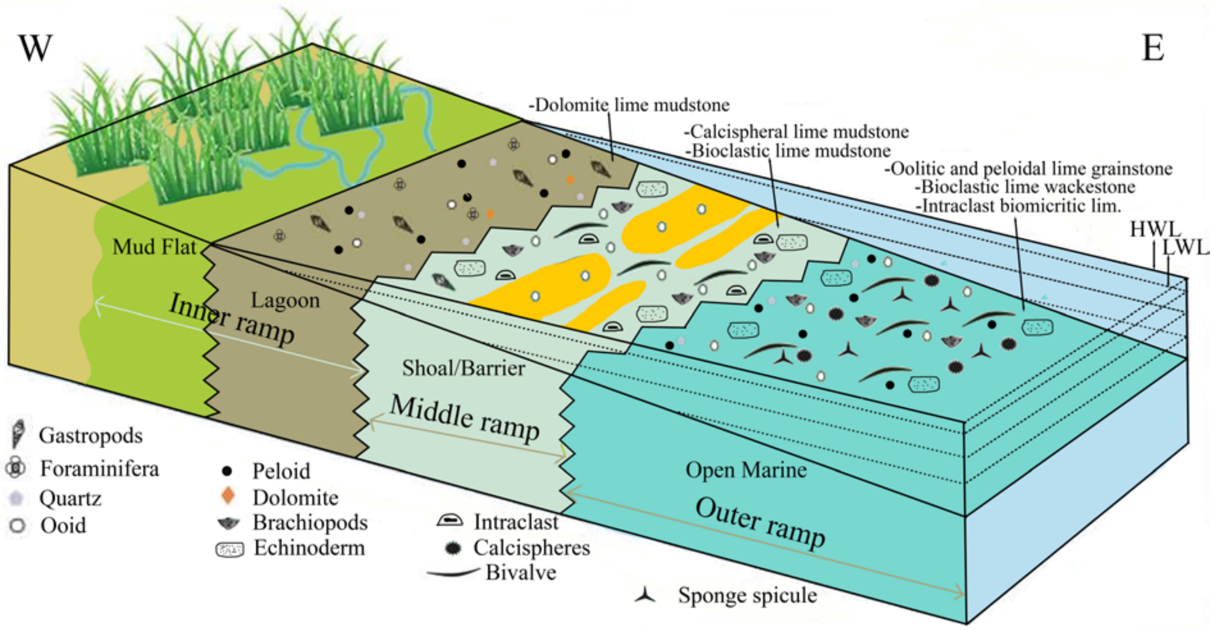

Text-fig. 13. A ramp model illustrating the Khasib Formation's depositional environment in central Iraq.

rable with the prior Turonian and Coniacian temperature trend. Multiple biological blooms were produced as a result of this process, in which the temperature gradually became suitable for life (Ezampanah *et al*. 2021). The stagnant aquatic environment that increases the hydrogen index HI and decreases the oxygen index OI converts the lacustrine or marine environment to an euxinic or suboxic-anoxic environment, which activates bacteria to attack particulate organic matter by enzymes and convert them to amorphous organic matter AOM. The seawater temperature of the Khasib Formation became more conducive to life, causing the massive biological explosion that eventually resulted in a C isotope excursion over the Earth.

The rise in buried organic matter with the concurrent decrease in atmospheric $CO_2$ was caused by the light carbon isotope ($^{12}C$) preferring to enter the products of photosynthesis, enriching $^{13}C$ in the reservoir of dissolved inorganic carbon. The biological explosion brought on by the temperature dropping to a level conducive to biological survival may be connected to the LTCE. Although broad suboxic-anoxic conditions were present and the Turonian–Coniacian marine redox boundary changed somewhat (Text-fig. 10; Ruidas and Zijlstra 2022), this is inconsistent with the outcomes of a biological expansion. This might be because there was an exceptionally high quantity of $CO_2$ in the atmosphere (approximately 4–5 times the amount now). Additionally, the equator-to-pole temperature differential was lowered to 35°C (Hay 2008), which delayed the global thermohaline circulation and ultimately made it impossible for surface-dissolved oxygen to flow downward. The oxygen cycle in the volume of water was retarded by the high paleotemperature (perhaps greater than 30°C), and biological abundance (Text-figs 3B, C and 13) encouraging increased consumption of the oxygen dissolved in seawater, resulting in decreasing circumstances.

## CONCLUSIONS

Elemental, isotopic, and lithological analyses have been used to show that the Khasib Fm in the East Baghdad Oilfield is primarily developed of intraclast biomicritic limestone, bioclastic lime mudstone, calcispheral lime mudstone, bioclastic lime wackestone, oolitic and peloidal lime grainstone, and dolomite lime mudstone. The paleotemperature at the time of deposition was approximately 28ºC, and the seawater salinity was low. The trace element ratios and Ce anomaly suggest that suboxic-anoxic conditions were present during the precipitation of the carbonate rocks in the Khasib Formation. The burying and preservation of organic materials were encouraged by the abundance of plankton, photosynthesis beneath the seawater surface, and the considerable suboxic-anoxic conditions. The Khasib Fm's seawater temperature was more conducive to life, causing a massive biological explosion that eventually resulted in a C isotope excursion over the Earth.

## Acknowledgements

The author expresses sincere gratitude to the Iraqi Oil Exploration Company and Midland Oil Company for supplying the essential data and cores. I want to sincerely thank the Ministry of Science and Technology s laboratory technicians for carrying out the experiments for this study. The author also appreciate the anonymous reviewers thorough evaluations and helpful recommendations of the work.

## REFERENCES

Al-Ameri, T.K. and Al-Obaydi, R.Y. 2011. Cretaceous petroleum system of the Khasib and Tannuma oil reservoir, East Baghdad oil field, Iraq. *Arabian Journal of Geosciences*, **4**, 915–932. DOI: 10.1007/s12517-009-0115-4

Al-Ameri, T., 2011. Khasib and Tannuma oil sources, East Baghdad oil field, Iraq. *Marine and Petroleum Geology*, 28, 880–894. DOI:10.1016/j.marpetgeo.2010.06.003

Al-Hamdani, A.M. 1986. Stratigraphy and geochemistry of Khasib, Tanuma and Saadi Formations in East Baghdad Oilfield, Central Iraq. Unpublished Ph.D. Thesis, 324 pp. College of Science, University of Baghdad; Baghdad.

AL-Tamimi, A.K.H. 2014. Hydrocarbon characterization and affinities of East Baghdad oil field, Iraq. Unpublished M.Sc. Thesis, 149 pp, College of Science, University of Baghdad; Baghdad.

Abdel-Fattah, M.I., Mahdi, A.Q. and Theyab, M.A. 2022. Lithofacies classification and sequence stratigraphic description as a guide for the prediction and distribution of carbonate reservoir quality: A case study of the Upper Cretaceous Khasib Formation (East Baghdad oilfield, central Iraq). *Journal of Petroleum Science and Engineering*, **209**, 109835.

Ali, R.A. 2023a. Geochemistry and Paleoredox Conditions of the Carbonate Reservoir Khasib Formation in East Baghdad Oilfield-Central Iraq. *Journal of Petroleum Research and Studies*, **41**, 16–36.

Ali, R.A. 2023b. Dolomitization mechanism of Pila Spi formation (middle–late Eocene) in the high folded zone, Northern Iraq. *Kuwait Journal of Science*, **50**, 105–114.

Ali, R.A. 2023c. Petrography and Geochemistry of Zubair Shale Formation in Rumaila Oilfield, Southern Iraq: Implications for Provenance and Tectonic Setting. *Journal of Petroleum Research and Studies*, **13,** Issue 40, 19–40.

Ali, R.A. and Jassim, H.K. 2023. Sedimentology and geochemistry of Zubair Formation sandstone reservoir, East Baghdad Oilfield, central Iraq. *Kuwait Journal of Science,* **50**, 427–437.

Al-Qayim, B. 2010. Sequence Stratigraphy and Reservoir Characteristics of the Turonian–Coniacian Khasib Formation in Central Iraq. *Journal of Petroleum Geology London*, **33**, 387–404.

Berner, R. A. and Kothavala, Z. 2001. Geocarb III: A Revised Model of Atmospheric $CO_2$ over Phanerozoic Time. *American Journal of Science*, **301**, 182–204.

Besen, R.M., Achilles, M., Alivernini, M., Voigt, P.F. and Struck, U. 2022. Stratigraphy and palaeoenvironments in the upper Turonian to lower Coniacian of the Saxonian Cretaceous Basin (Germany) – insights from calcareous and agglutinated foraminifers. *Acta Geologica Polonica*, **72**, 159–186.

Bice, K. L., Huber, B. T. and Norris, R. D. 2003. Extreme polar warmth during the Cretaceous greenhouse? Paradox of the late Turonian $\delta\ ^{18}O$ record at Deep Sea Drilling Project Site 511. *Paleoceanography*, **18**, 1031.

Bolhar, R. and Van Kranendonk, M.J. 2007. A non-marine depositional setting for the northern Fortescue Group, Pilbara Craton, inferred from trace element geochemistry of stromatolitic carbonates. *Precambrian Research*, **155**, 229e250..

Bromhead, A. D., Van Buchem, F.S.P., Simmons M.D. and Davies, R.B. 2022. Sequence stratigraphy, palaeogeography and petroleum plays of the Cenomanian–Turonian succession of the Arabian Plate: An updated synthesis. *Journal of Petroleum Geology*, **45**, 119–162.

Chen, G., Sun, Z., Nie, F., Li, C., Zhen, Y. and Zhou, Z. 2020. Hydrogeochemical characteristics of the sandstone-hosted uranium mineralization in northern Ordos Basin, China. *Ore Geology Reviews*, **126**, 103769.

Colín-Rodríguez, A., Núnez-Useche, F. and Adatte, T. 2023. The expression of late Cenomanian–Coniacian episodes of accelerated global change in the sedimentary record of the Mexican Interior Basin. *Cretaceous Research*, **143**, 105380.

Duda, P., Blumenberg, M. and Thiel, V. 2014. Geobiology of a palaeoecosystem with Ediacara-type fossils: the Shibantan member (Dengying Formation, South China). *Precambrian Res*earch **255**, 48e62.

Eldrett, J. S., Ma, C., Bergman, S. C., Lutz, B. and Gregory, F.J. 2015. An astronomically calibrated stratigraphy of the Cenomanian, Turonian and earliest Coniacian from the Cretaceous Western Interior Seaway, USA: Implications for global chronostratigraphy. *Cretaceous Research*, **56**, 316–3440.

Ezampanah, Y., Scopelliti, G., Sadeghi, A. and Adabi, M.H. 2021. Turonian–Maastrichtian biostratigraphy and isotope stratigraphy of the Kopet-Dagh Basin deposits, northeastern Neo-Tethys, Iran. *Palaeogeography, Palaeoclimatology, Palaeo*cology, **581**, 110605.

Fayadh, A.H. and Nasser, M.E. 2018. 3D Geological Model for Khasib, Tanuma, and Sa'di formations of Halfaya Oil

Field in Missan Governorate-Southern Iraq. *Iraqi Journal of Science*, **59**, 875–885

Frijia, G., Parente, M., Lucia, M. and Mutti, M. 2015. Carbon and strontium isotope stratigraphy of the Upper Cretaceous (Cenomanian–Campanian) shallow-water carbonates of southern Italy: Chronostratigraphic calibration of larger foraminifera biostratigraphy. *Cretaceous Research*, **53**, 110–139.

Flügel, E. 1982. Microfacies Analysis of Limestone, 633 pp. Springer-Verlag; New York,

Huber, B.T., MacLeod, K.G., Watkins, D.K. and Coffin, M.F. 2018. The rise and fall of the Cretaceous Hot Greenhouse climate. *Global and Planetary Change*, **167**, 1–23.

Gayara, A.D. and Al Khaykanee, M.H. 2015. Paleoenvironments and Sequence Stratigraphy of the Turonian–Lower Campanian Succession at Majnoon Oil Field, Southern Iraq. *Iraqi Journal of Science*, **56**, 2880–2886.

Geerken, E., Nooijer, L.J. and Dijk, I.V. 2018. Impact of salinity on element incorporation in two benthic foraminiferal species with contrasting magnesium contents. *Biogeosciences*, **15**, 2205e22188.

Gundogar, D.Y. and Sasmaz, A., 2022. Geochemical Approach to Determine the Possible Precipitation Parameters of the Coniacian–Santonian Mazidagi Phosphates, Mardin, Turkey. *Minerals*, **12**, 1544.

Hay, W.W. 2008. Evolving ideas about the Cretaceous climate and ocean circulation. *Cretaceous Research*, **29**, 725–753.

Jaffrés, J.B.D., Shields, G.A. and Wallmann, K. 2007. The oxygen isotope evolution of seawater: A critical review of a long-standing controversy and an improved geological water cycle model for the past 3.4 billion years. *Earth Science Reviews*, **83**, 83–122.

Jameel, L.A., Kadhim, F.S. and Al-Sudani, H.I. 2020. Geological Model for Khasib Formation of East Baghdad Field Southern Area. *Journal of Petroleum Research and Studies*, **28** (9), E21–E35.

Jarvis, I., Gale, A. S., Jenkyns, H.C. and Pearce, M.A. 2006. Secular variation in Late Cretaceous carbon isotopes: a new $\delta^{13}C$ carbonate reference curve for the Cenomanian–Campanian (99.6–70.6 Ma). *Geological Magazine*, **143**, 561–608.

Jarvis, I., Alexandre, J.T., Grocke, D.R., Ulicny, D. and Laurin, J., 2015. Intercontinental correlation of organic carbon and carbonate stable isotope records: evidence of climate and sea-level change during the Turonian (Cretaceous). *The Depositional Record*, **1**, 53–90.

Jeans, C.V., Wray, D.S., Williams, C.T., Bland, D.J. and Wood, C.J., 2021. Redox conditions, glacio-eustasy, and the status of the Cenomanian–Turonian Anoxic Event: new evidence from the Upper Cretaceous Chalk of England. *Acta Geologica Polonica*, **71**, 103–152.

Jiu, B., Huang, W. and Mu, N. 2021. Types and controlling factors of Ordovician paleokarst carbonate reservoirs in the southeastern Ordos Basin, China. *Journal of Petroleum Science and Engineering*, **198**, 108162.

Jones, B. and Manning, D.A.C. 1994. Comparison of geochemical indices used for the interpretation of paleoredox conditions in ancient mudstones. *Chemical Geology*, **114**, 111e129.

Joo, Y.J. and Sageman, B.B. 2014. Cenomanian to Campanian carbon isotope chemostratigraphy from the Western Interior Basin. *Journal of Sedimentary Research*, **84**, 529–542.

Hussain, S.H., Al-Juboury, A.I., Al-Haj, M.A., Armstrong-Altrin, J.S. and Al-Lhaebi, S.F., 2021. Mineralogy and geochemistry of the Late Triassic Baluti Formation, Northern Iraq. *Journal of African Earth Sciences*, **181**, 104243.

Krabbenhoft, A., Eisenhauer, A. and Bohm, F. 2010. Constraining the marine strontium budget with natural strontium isotope fractionations ($^{87}Sr/^{86}Sr^*$, $\delta^{88}/^{86}Sr$) of carbonates, hydrothermal solutions, and river waters. *Geochem. Coscmochim. Acta*, **74**, 4097e4109.

Lash, G.G. 2018. Significance of stable carbon isotope trends in carbonate concretions formed in association with anaerobic oxidation of methane (AOM), Middle and Upper Devonian shale succession, western New York State, USA. *Marine and Petroleum Geology*, **91**, 470e479.

Li, C., Wu, H. and Chu, Z. 2019. Precise determination of radiogenic Sr and Nd isotopic ratios and Rb, Sr, Sm, Nd elemental concentrations in four coal ash and coal fly ash reference materials using isotope dilution thermal ionization mass spectrometry. *Microchemical Journal*, **146**, 906e913.

Li, H., Zhang, S., Han, J. and Zhong, T. 2022. Astrochronologic calibration of the Shuram carbon isotope excursion with new data from South China. *Global and Planetary Change*, **209**, 103749.

Linnert, C., Robinson, S.A., Lees, J.A., Pérez-Rodríguez, I., Jenkyns, H.C., Jenkyns, H.C., Petrizzo, M.R., Arz, J.A., Bown, P.R. and Falzoni, F. 2018. Did Late Cretaceous cooling trigger the Campanian–Maastrichtian Boundary Event? *Newsletters on Stratigraphy,* **51**, 145–166.

McArthur, J.M. and Howarth, R.J. 2024. Strontium isotope stratigraphy of the Cretaceous. *Geological Society, London, Special Publications*, **544**, 343–366.

Mehrabi, H., Yahyaei, E., Navidtalab, A., Rahimpour-Bonab, H., Abbasi, R., Omidvar, M., Assadi, A. and Honarmand, J. 2023. Depositional and diagenetic controls on reservoir properties along the shallow-marine carbonates of the Sarvak Formation, Zagros Basin: Petrographic, petrophysical, and geochemical evidence. *Sedimentary Geology*, **454**, 106457.

Mohammed, A., Dhaidan, M. and Al-Hazaa, S.H. 2022. Reservoir characterization of the upper Turonian–lower Coniacian Khasib formation, South Iraq: Implications from electrofacies analysis and a sequence stratigraphic framework. *Journal of African Earth Sciences*, **186**, 104431.

Morse, J.W. and Mackenzie, F.T. 1990. Geochemistry of Sedimentary Carbonates. *Developments in Sedimentology*, **48**, 373–446.

O'Neil, J.R., Clayton, R.N. and Mayeda, T.K. 1969. Oxygen Isotope Fractionation in Divalent Metal Carbonates. *The Journal of Chemicla Physica*, **51** (12), 5547–5558.

Prasanta, K.M. and Sarada, P.M. 2021. Geochemistry of carbonate rocks of the Chilpi group, Bastar Craton, India: implications on ocean paleoredox conditions at the late paleoproterozoic era. *Precambrian Research***, 353**, 106023.

Ren, Y., Zhong, D. and Gao, C. 2019. The paleoenvironmental evolution of the Cambrian Longwangmiao Formation (stage 4, Toyonian) on the Yangtze platform, South China: petrographic and geochemical constrains. *Marine and Petroleum Geology*, **100**, 391e411.

Ruidas, D.K. and Zijlstra, J.J.P. 2023. The hardgrounds of the Turonian–Coniacian carbonates of the Bagh Group of central India. *Journal of Earth System Science*, **132**, 27.

Salmouna, D.J., Chaabani, F., Dhahri, F., Mzoughi, M., Salmouna, A. and Zijlstra, H.B. 2014. Lithostratigraphic analysis of the Turonian–Coniacian Bireno and Douleb carbonate Members in Jebels Berda and Chemsi, Gafsa basin, central-southern Atlas of Tunisia. *Journal of African Earth Sciences*, **100**, 733–754.

Saltzman, M.R. and Edwards, C.T. 2017. Gradients in the carbon isotopic composition of Ordovician shallow water carbonates: A potential pitfall in estimates of ancient $CO_2$ and $O_2$. *Earth and Planetary Science Letters*, **464**, 46–54.

Sarangi, S. Mohanty, S.P. and Barik, A. 2017. Rare earth element characteristics of Paleoproterozoic cap carbonates pertaining to the Sausar Group, Central India: implications for ocean paleoredox conditions. *Journal of Asian Earth Sci*ence, **148**, 31e50.

Sharland, P.R., Archer, R., Casey, D.M., Davies, R.B., Hall, S., Heward, A., Horbury, A. and Simmons, M.D., 2001. Arabian Plate Sequence Stratigraphy. *GeoArabia Special Publication*, **2**, 1–387. Gulf PetroLink.

Steuber, T. 2001. Strontium isotope stratigraphy of Turonian–Campanian Gosau-type rudist formations in the Northern Calcareous and Central Alps (Austria and Germany). *Cretaceous Research*, **22**, 429–441.

Tarduno, J.A., Brinkman, D.B., Renne, P.R., Cottrell, R.D., Scher, H. and Castillo, P. 1998. Evidence for extreme climatic warmth from Late Cretaceous Arctic vertebrates. *Science*, **282**, 2241–2243.

Total, C.F. 1984. Sedimentation and diagenesis study of Tanuma and Khasib reservoirs, synthesis of the available core data, 98 pp. Interim report, INOC Library; Baghdad.

Tukkee, I.Q.H., Hussain, S.A. and Sahaab, A.M. 2023. Reservoir Characteristics for Khasib Formation in selected wells of East Baghdad Oil field, Iraq. *Iraqi Journal of Science*, **64**, 4502–4517.

Turgeon, S. and Brumsack, H.-J. 2006. Anoxic vs dysoxic events reflected in sediment geochemistry during the Cenomanian–Turonian Boundary Event (Cretaceous) in the Umbria-Marche Basin of central Italy. *Chemical Geology*, **234**, 321–339.

Wang, Q., Wen, T., Li, H., Zeng, X., Wang, X., Xin, J. and Sun, L. 2022. Influence of heterogeneity on fluid property variations in carbonate reservoirs with multistage hydrocarbon accumulation: A case study of the Khasib formation, Cretaceous, AB oilfield, southern Iraq. *Open Geosciences*, **14**, 663–674.

Wilson, P.A., Norris, R.D. and Cooper, M.J. 2002. Testing the Cretaceous greenhouse hypothesis using glassy foraminiferal calcite from the core of the Turonian tropics on Demerara Rise. *Geology*, **30**, 607–610.

Yang, J.-Q., Zhang, J.-T., He, Z.-L. and Zhang, T. 2023. Paleoenvironment reconstruction of the Middle Ordovician thick carbonate from western Ordos Basin, China. *Petroleum Science*, **20**, 48–59.

Zhang, K. and Shields, G.A. 2022. Sedimentary Ce anomalies: Secular change and implications for paleoenvironmental evolution. *Earth-Science Reviews*, **229**, 104015.

*Manuscript submitted: 18th November 2024*
*Revised version accepted: 25th March 2025*